Spectroscopic definition of ferrous active sites in non-heme iron enzymes

Edward I. Solomon[1,2,*], **Robert R. Gipson**[1]

[1]Department of Chemistry, Stanford University, Stanford, California 94305-5080

[2]Stanford Synchrotron Radiation Lightsource, SLAC National Acceleration Laboratory, Stanford University, Mento Park, California 94025

Abstract

Non-heme iron enzymes play key roles in antibiotic, neurotransmitter, and natural product biosynthesis, DNA repair, hypoxia regulation, and disease states. These had been refractory to traditional bioinorganic spectroscopic methods. Thus, we developed variable-temperature variable-field magnetic circular dichroism (VTVH MCD) spectroscopy to experimentally define the excited and ground ligand field states of non-heme ferrous enzymes (Solomon et al., 1995). This method provides detailed geometric and electronic structure insight and thus enables a molecular level understanding of catalytic mechanisms. Application of this method across the five classes of non-heme ferrous enzymes has defined that a general mechanistic strategy is utilized where O_2 activation is controlled to occur only in the presence of all cosubstrates.

Keywords

Non-heme iron enzymes; magnetic circular dichroism spectroscopy; ligand field theory; non-Kramers' ions; saturation magnetization; ferrous enzyme mechanisms

The five major classes of mononuclear non-heme iron (NHFe) enzymes, presented in Table 1, use a high spin ferrous site to activate dioxygen (Solomon et al., 2000). The non-cofactor dependent enzymes on the left, the cysteine oxidases and oxygenases (Baldwin & Abraham, 1988; Fernandez et al., 2022), the Rieske dioxygenases (Barry & Challis, 2013), and the diol dioxygenases (Lipscomb, 2008; Vaillancourt et al., 2006) have all been determined to react through high-spin ferric-superoxo intermediates that electrophilically attack their bound substrate (Babicz et al., 2023; Goudarzi et al., 2018; Sutherlin, S. Rivard, et al., 2018; Sutherlin, Wasada-Tsutsui, et al., 2018). In the cofactor dependent enzymes (cofactor = α-ketoglutarate (αkg) and pterin), the cofactor and the Fe(II) active site together transfer 4 electrons to O_2 to generate Fe(IV)=O S=2 intermediates (Krebs et al., 2007). For the αkg dependent enzymes, this intermediate H-atom abstracts (HAA) from its substrate and then rebound hydroxylates, halogenates, or desaturates the subsequent substrate radical (Blasiak et al., 2006; Purpero & Moran, 2007), while in the pterin dependent NHFe enzymes, the

*Corresponding author (edward.solomon@stanford.edu).

Fe(IV)=O S=2 intermediate performs electrophilic aromatic substitution (EAS) on their aromatic amino acid substrates (Fitzpatrick, 2023; Kappock & Caradonna, 1996).

Non-heme ferrous metalloenzymes are much more challenging to spectroscopically study than heme enzymes as they do not exhibit the intense $\pi \rightarrow \pi^*$ transitions of the porphyrin. As shown in Figure 1, these NHFe enzymes generally have a non-chromophoric facial triad set of two histidine and one carboxylate ligand (Kal & Que, 2017), or for the αkg dependent halogenases the carboxylate is replaced by the halide (Cl^-, Br^-) (Blasiak et al., 2006), with the remaining Fe(II) coordination positions occupied by H_2O's from solvent. Also, these ferrous active sites do not exhibit the low-energy, intense ligand to metal charge transfer features exhibited by ferric sites, and as these are d^6 even electron ions, they have integer spin non-Kramers' ground states that are generally not accessible by X-band EPR (as described below). However, high spin ferrous sites do have $d \rightarrow d$ transitions that are well described by ligand field theory.

d^6 Ligand Field Theory (LFT)

The Tanabe-Sugano (T&S) diagram in Figure 2 gives the energies of all the ligand field (LF) states of an octahedral d^6 ion that are dependent on the combined effects of the ligand field splittings of the d-orbitals (10 Dq) and the repulsions between the electrons within these orbitals (quantified by the Racah parameter B) (Solomon & Hanson, 2006). For a high spin ferrous octahedral site, the left side of this T&S diagram is appropriate, which shows that the ground state is a $^5T_{2g}$ with the extra electron in one of the three-fold degenerate t_{2g} orbitals. There is one spin allowed ligand field transition from this ground state to the ^5E_g excited state that corresponds to the extra electron promoted into the two-fold degenerate e_g set of d orbitals. As shown in this T&S diagram (Figure 2) and on the left in Figure 3, this transition is at an energy of 10 Dq (the LF splitting energy of the two-fold degenerate e_g above the three-fold degenerate t_{2g} orbitals) that for the facial triad ligation is approximately 10,000 cm^{-1}.

As shown in Figure 3, the two-fold orbital degeneracy of the ^5E_g excited state is predicted by LFT to split in energy in a characteristic way dependent on the active site coordination number and structure (Pavel et al., 1998). For distorted 6 coordinate (6C) high spin ferrous protein sites, the ^5E excited state can split by up to approximately 2,000 cm^{-1}, predicting 2 spin-allowed LF transitions, from the lowest energy component of the ground state to these ^5E derived excited states, at approximately 10,000 cm^{-1} split by up to 2,000 cm^{-1}. Removing one ligand to generate a square pyramidal, 5C structure predicts a large splitting of the ^5E state with spin allowed LF transitions at >10,000 and at approximately 5,000 cm^{-1}. Distortion of the 5C structure to trigonal bipyramidal changes the LF and somewhat lowers the energy of both transitions, still predicting a splitting of ~5,000 cm^{-1}. Removal of another ligand generates a 4C distorted tetrahedral Fe(II) site. From LFT, 10 Dq (tetrahedron) = (−4/9) 10 Dq (octahedron), thus predicting only low energy spin allowed $d \rightarrow d$ transitions in the 5,000–7,000 cm^{-1} energy region.

LF Spectroscopy = Low Temperature Magnetic Circular Dichroism (LT MCD)

From the summary above, electronic spectroscopy in the ligand field region is a very sensitive probe of high spin ferrous active site structure. However, these spin-allowed transitions (Figure 3) are still parity forbidden (d→d), thus very weak in absorption ($\varepsilon \sim 10$ M^{-1} cm^{-1}). Additionally, they are in the near infrared (NIR) 12,000 – 4,000 cm^{-1} spectral region that is obscured by intense overlapping vibrational transitions of the protein and solvent. Thus, the ferrous enzyme LF transitions are not accessible by absorption spectroscopy. However, the high spin Fe(II) ground state is an S = 2, quintet that is paramagnetic. The way to study paramagnetic metal ion active sites is by MCD at low temperatures, due to the C-term intensity mechanism (Buckingham & Stephens, 1966) explained below, where at low temperatures, paramagnetic MCD signals are two to three orders of magnitude more intense than those of the diamagnetic background. As shown in Figure 4, MCD spectroscopy involves the differential absorption of left versus right circularly polarized (LCP vs. RCP) light induced by a longitudinal magnetic field of up to 7 T at temperatures down to 1.6 K, where LCP light has its $\overrightarrow{E}$ vector rotating counterclockwise as it propagates to the detector and RCP rotates clockwise.

We have measured the low temp LF MCD spectra of more than 20 structurally defined mononuclear high spin Fe(II) complexes, and the predictions of LFT (Figure 3) are strongly supported by experiment (Pavel et al., 1998). Figure 5 presents representative LT MCD spectra for each structural type. 6C shows two LF transitions in the ~10,000 cm^{-1} region, split by approximately 2,000 cm^{-1}; 5C square pyramidal sites show transitions at >10,000 cm^{-1} and ~5,000 cm^{-1}; for trigonal bipyramidal, these shift to lower energies still with an ~5,000 cm^{-1} splitting; and 4C distorted tetrahedral Fe(II) sites show only low energy LF transitions in the 5,000 – 7,000 cm^{-1} region. Note that while MCD transitions can be either positively or negatively signed, most LF transitions of high spin ferrous active sites exhibit transitions of the same sign (positive bands in Figure 5) in MCD due to the presence of low lying LF excited states that spin-orbit couple with the ground state leading to this "deviation from the sum rule" (Gerstman & Brill, 1985; Solomon & Hanson, 2006).

Variable-Temperature, Variable-Field (VTVH) MCD

It is important to also observe in Figure 3, that the three-fold orbital degeneracy of the $^5T_{2g}$ ground state (deriving from the extra electron in the t_{2g} set of d orbitals) is also split in energy due to differences in π bonding interactions with the ligands in the different coordination geometries. We have derived a method to obtain this splitting from the temperature (T) and field (H) dependence of the MCD intensity (VTVH MCD) of the LF transitions (Whittaker & Solomon, 1988). Figure 6A shows the field dependence of the MCD intensity at 4.2 K for a 5C square pyramidal complex as in Figure 5. The intensity of the bands increases in a nonlinear way with increasing field (and decreasing temperature) and levels off at high fields and low temperatures. This saturation magnetization behavior is shown in Figure 6B (left to right), where the intensity first increases linearly by orders of magnitude with increasing field and decreasing temperature. This is the C-term behavior of paramagnetic systems (Buckingham & Stephens, 1966). Then at very high field and low temperature, the MCD intensity levels off and is saturated (Schatz et al., 1978; Solomon &

Hanson, 2006; Stephens, 1976; Thomson & Johnson, 1980). The origin of this saturation magnetization behavior can be understood by first considering the simplest $S = \frac{1}{2}$ Kramers' doublet system in the inset of Figure 6B. Both the ground state and the excited state are two-fold spin degenerate ($M_s = \pm\frac{1}{2}$) and this is split in energy by the magnetic Zeeman effect. Two transitions from the ground to the excited state of equal magnitude but opposite sign are allowed by the $M = \pm1$ selection rule of MCD. Note that these Zeeman energy splittings at high magnetic fields are a few wavenumbers while the transition band shapes have full-width at half-maxima of ~1,000 cm^{-1}. Thus at high temperatures and low magnetic fields, the ground state sublevels are equally populated and these transitions cancel leading to the very low MCD intensity at the left of the saturation magnetization curve in Figure 6B. As the field increases and the temperature decreases (increasing H/T from left to right), the higher energy sublevel of the ground state loses Boltzmann population; thus, the transition probability from this sublevel decreases, cancellation no longer occurs, and the intensity initially increases linearly with H/T (the C-term MCD mechanism, $\beta H/2kT = 0$ to ~0.4 in Figure 6B). Finally, when the field is further increased and temperature decreased, only the lowest $M_s = -\frac{1}{2}$ sublevel is populated and the MCD intensity is saturated (at $\beta H/2kT \sim 1.0$ in Figure 6B).

For an $S = \frac{1}{2}$ Kramers' ion, saturation magnetization curves of the MCD intensity of a specific band obtained at different fixed temperatures (with varying fields from 0 to 7T for each temperature) all superimpose when plotted versus H/T as in Figure 6B, a behavior described by the Brillouin function for an $S = 1/2$ system (equation 1) (Solomon & Hanson, 2006):

$$I = \frac{1}{2}NgB \ \tanh(g\beta H/2kT)$$

(eqn. 1)

However, when saturation magnetization curves are obtained for an $S = 2$ non-Kramers' Fe(II) active site, there is a spread or nesting of these curves (each with a fixed temperature and varying field) as shown in Figure 7A. Insight into the origin of this nesting behavior was obtained by uncoupling the temperature and field variables, thus plotting the MCD intensity with decreasing temperature for fixed magnetic fields that were incrementally increased. This plot is presented in Figure 7B, which shows that the saturation of MCD intensity at low temperature for each magnetization curve increases with increasing magnetic field eventually leveling off at high field. This increase of intensity at saturation requires that the wavefunction of the lowest component of the ground state changes with magnetic field. This behavior led us to the **non-Kramers' doublet model for saturation magnetization** presented below (Whittaker & Solomon, 1988).

When the spin of the ground state is greater than 1/2, its 2S+1 spin degeneracy in M_s (=0, ±1, ±2) will split in energy even in the absence of a magnetic field when the metal site symmetry is lower than octahedral or tetrahedral. This zero field splitting (ZFS) of an $S = 2$ with a negative axial (D) and then rhombic (E) distortion of the LF is shown on the left in Figure 8. It is important to observe that for an integer spin non-Kramers' ion, the doublets are split in energy by the rhombic LF even in the absence of a magnetic field; the ±2 doublet

is split by δ in the middle of Figure 8. δ is generally larger than the microwave energy at X-band which is the origin of the lack of an EPR signal for non-Kramers' ions. However, this is also the origin of the nesting in the saturation magnetization curves in Figure 7. As shown on the right of Figure 8, in addition to the rhombic splitting of the $M_s = \pm 2$ by δ, the wavefunctions also equally mix eliminating their spin expectations, and therefore their MCD signals which depend on this, at zero and low magnetic fields. However, as the field is increased in addition to the Zeeman splitting of the sub-levels (by $g_\parallel \beta H \cos\theta$) the wavefunctions also change, becoming pure $M_s = -2$ (and +2) and MCD active at high magnetic fields. The MCD intensity expression for this non-Kramers' behavior is given by equation 2 (Solomon et al., 1995; Whittaker & Solomon, 1988):

$$I_{MCD} = A_{SatLim} \int_0^{\pi/2} \frac{cos^2\theta sin\theta}{\sqrt{\delta^2 + (g_\parallel \beta H cos\theta)^2}} (g_\parallel \beta H) \cdot tanh\left[\frac{\sqrt{\delta^2 + (g_\parallel \beta H cos\theta)^2}}{2kT}\right] d\theta$$

(eqn. 2)

The saturation magnetization data in Figure 7 can be fit using the non-Kramers' doublet equation 2 with orientation averaging for a frozen protein solution to obtain experimental values for δ and $g_\parallel$ in Figure 8. Thus, we use an excited state to study the ground state and obtain EPR parameters from an EPR inactive site. Note that Figure 8 considers the case of a negative ZFS. The positive ZFS case gives equivalent behavior and involves a parallel analysis as presented by Campochiaro et al. and Solomon et al. (Campochiaro et al., 1995; Solomon et al., 1995).

LFT of Spin-Hamiltonian Parameters from VTVH MCD

We now relate the δ and $g_\parallel$ obtained from the VTVH MCD data in Figure 7 to the axial ( ) and rhombic (V) split set of t_2 $d\pi$ orbitals in Figure 9A. Low symmetry distortion from octahedral can only split orbital degeneracy, thus ZFS of a spin degeneracy must derive from spin-orbit coupling (SOC). While for many transition metal sites (e.g. high spin Fe(III)) this involves out-of-state SOC which has a number of contributions limiting its utility, for high spin Fe(II) sites the $^5T_{2g}$ has dominantly in-state SOC and its analysis is direct and insightful. The $^5T_{2g}$ ground state is three-fold orbitally degenerate (extra electron can be in the d_{xy}, d_{yz}, or d_{xz} orbital) and this behaves as having an effective orbital angular momentum of 1. This SOCs to the S=2 giving the spin orbit split (by 2λ and 3λ, where λ is the T_{2g} state SOC parameter that is approximately -80 cm^{-1} for Fe(II) (Solomon et al., 1995)) levels at the left in Figure 9B. Proceeding from left to right in Figure 9B, SOC is combined with the axial and rhombic splitting of the t_2 $d\pi$ orbitals (from Figure 9A) and finally the Zeeman effect in the expanded inset. Thus, from LFT including in-state SOC we can relate the δ and $g_\parallel$ obtained experimentally from the VTVH MCD saturation magnetization curves (Figure 7) to the axial ( ) and rhombic (V) splitting of the $d\pi$ orbitals (Figure 9A). These correlations are given in Figure 10. Thus for the four complexes in Figure 5, we can experimentally obtain the energy splittings of their five d orbitals (Figure 11). Thus, we have developed a spectroscopic probe of the geometric and electronic structures of non-heme ferrous active sites and can now use NIR VTVH MCD to obtain molecular level insight into catalytic mechanisms.

An Early Application of VTVH MCD on a Non-Heme Fe(II) Enzyme

Phenylalanine hydroxylase (PAH) is a pterin dependent non-heme iron enzyme (Table 1) that is familiar to the reader because of the warning on diet soda cans concerning phenylketonuria (PKU). This is a genetic disease where a mutation in PAH leads to poor catalysis and a buildup of phenylalanine resulting in brain damage (Erlandsen et al., 2003). We studied the VTVH MCD of this enzyme in collaboration with J. Caradonna (Kemsley et al., 1999, 2003). Figure 12A panel I (black solid line) gives the LT MCD spectrum of resting Fe(II) PAH; two LF transitions at ~10,000 cm^{-1}, split by ~2,000 cm^{-1} indicating a 6C active site. Substrate binding leads to the black dotted MCD spectrum; this shows only a small perturbation of the LF transitions indicating that the substrate binding in the protein pocket results in only a small change of the 6C Fe(II) site (panel I, dotted). Panel II shows that there is no effect of the pterin on the Fe(II) (panel II, dashed) indicating that this cofactor does not bind to the Fe(II) in the absence of substrate. Importantly in panel III, substrate and cofactor together bind to PAH to produce a large change in the LF MCD spectrum (gray), now with one transition at ~10,000 cm^{-1} and a second lower energy transition at <5,500 cm^{-1} indicating that the Fe(II) site in PAH has gone 5C. This behavior is also observed in the VTVH MCD data on PAH in Figure 12B where there is a large change in the saturation magnetization curves with substrate plus cofactor binding to the active site (right). Analyses of the VTVH MCD data in Figure 12A and B give the experimental splittings of the Fe(II) five 3d orbitals of PAH shown in Figure 12C. In going from left to right with substrate plus cofactor binding, 10 Dq goes down and there is a large low symmetry splitting of the t_2 and e sets of d orbitals all demonstrating that the PAH active site has become 5C.

We have observed parallel behavior over the five classes of mononuclear non-heme ferrous enzymes in Table 1 (Neidig & Solomon, 2005; Solomon et al., 2000), presented specifically for the cofactor dependent enzymes in Figure 13. The resting ferrous site, the Fe(II) site with substrate, and the Fe(II) site with cofactor are all 6C, coordinately saturated and relatively stable in the presence of dioxygen. However, when both the substrate and cofactor are simultaneously bound to the enzyme, the Fe(II) site becomes 5C (via loss of an H_2O ligand (Light et al., 2014)) and able to react with O_2 only in the presence of both co-substrates to generate the Fe(IV)=O intermediate for the efficient coupled reaction with substrate.

Perspective

While this *Methods in Enzymology* article has focused on VTVH MCD of mononuclear non-heme ferrous enzymes, we note that VTVH MCD has also provided significant insight in a number of the binuclear non-heme ferrous enzymes that also activate dioxygen (Solomon & Park, 2016). There are two additional features concerning application of this method to binuclear ferrous enzymes. First, it is able to determine the exchange coupling (J) between the ferrous ions that directly defines the bridging ligation. This required the development of J/D diagrams (i.e. exchange/ZFS) that allow analysis of this coupling in the presence of the ZFS of both ferrous sites that can be comparable to J for biferrous sites (Solomon et al., 2000). In addition, each Fe(II) in principle exhibits two LF transitions in the NIR MCD spectrum (total of up to four) that can be associated to each other (i.e. two sets of two) through their VTVH behavior that directly reflects the contribution of each Fe(II) (i.e.

its M_s value) to the exchange coupled total ground state wavefunction enabling coordination structural assignment for each Fe(II) center (Neese & Solomon, 1999).

The reaction of the 5C, coordinately unsaturated Fe(II) sites defined for the five classes of mononuclear non-heme ferrous enzymes in Table 1 and for the correctly oriented coordinately unsaturated biferrous sites in the coupled binuclear non-heme iron enzymes (Park et al., 2017) by VTVH MCD generates oxygen intermediates that accomplish the wide range of chemistries noted in Table 1 and by Solomon and Park (Solomon & Park, 2016). To understand the mechanisms of these reactions, it is critical to use stopped-flow and rapid freeze quench methods to trap and then spectroscopically define their associated oxygen intermediates (Babicz et al., 2023; Mitić et al., 2007). As oxygen intermediates are oxidized and thus more spectroscopically accessible, a number of insightful spectroscopic methods have been and are being applied to elucidate the geometric and electronic structures of these intermediates (Solomon & Hanson, 2006). Here we emphasize that VTVH MCD on oxygen intermediates probe the low lying unoccupied or half-occupied orbitals that serve as the Frontier Molecular Orbitals (FMOs) enabling their overlap with substrate for electrophilic and HAA reactivity. One example is the π^* FMO of the Fe(IV)=O intermediate in the αkg dependent halogenases (Figure 14) (Srnec et al., 2016) that enables selective halogenation over the thermodynamically favored hydroxylation (Srnec & Solomon, 2017).

Acknowledgements:

References:

Babicz JT, Rogers MS, DeWeese DE, Sutherlin KD, Banerjee R, Böttger LH, Yoda Y, Nagasawa N, Saito M, Kitao S, Kurokuzu M, Kobayashi Y, Tamasaku K, Seto M, Lipscomb JD, & Solomon EI (2023). Nuclear Resonance Vibrational Spectroscopy Definition of Peroxy Intermediates in Catechol Dioxygenases: Factors that Determine Extra-versus Intradiol Cleavage. Journal of the American Chemical Society. 10.1021/JACS.3C02242

Baldwin JE, & Abraham E (1988). The biosynthesis of penicillins and cephalosporins. Natural Product Reports, 5(2), 129–145. 10.1039/NP9880500129 [PubMed: 3145474]

Barry SM, & Challis GL (2013). Mechanism and Catalytic Diversity of Rieske Non-Heme Iron-Dependent Oxygenases. ACS Catalysis, 3(10), 2362–2370. 10.1021/cs400087p

Blasiak LC, Vaillancourt FH, Walsh CT, & Drennan CL (2006). Crystal structure of the non-haem iron halogenase SyrB2 in syringomycin biosynthesis. Nature, 440(7082), 368–371. 10.1038/nature04544 [PubMed: 16541079]

Buckingham AD, & Stephens PJ (1966). Magnetic Optical Activity. Annual Review of Physical Chemistry, 17(1), 399–432. 10.1146/annurev.pc.17.100166.002151

Campochiaro C, Pavel EG, & Solomon EI (1995). Saturation Magnetization Magnetic Circular Dichroism Spectroscopy of Systems with Positive Zero-Field Splittings: Application to FeSiF6·6H2O. Inorganic Chemistry, 34(18), 4669–4675. 10.1021/IC00122A025

Erlandsen H, Patch MG, Gamez A, Straub M, & Stevens RC (2003). Structural Studies on Phenylalanine Hydroxylase and Implications Toward Understanding and Treating Phenylketonuria. Pediatrics, 112(Supplement 4), 1557–1565. 10.1542/peds.112.S4.1557 [PubMed: 14654665]

Fernandez RL, Juntunen ND, & Brunold TC (2022). Differences in the Second Coordination Sphere Tailor the Substrate Specificity and Reactivity of Thiol Dioxygenases. Accounts of Chemical Research, 55(17), 2480–2490. 10.1021/acs.accounts.2c00359 [PubMed: 35994511]

Fitzpatrick PF (2023). The aromatic amino acid hydroxylases: Structures, catalysis, and regulation of phenylalanine hydroxylase, tyrosine hydroxylase, and tryptophan hydroxylase. Archives of Biochemistry and Biophysics, 735, 109518. 10.1016/j.abb.2023.109518

Gerstman BS, & Brill AS (1985). Magnetic circular dichroism of low symmetry cupric sites. The Journal of Chemical Physics, 82(3), 1212–1230. 10.1063/1.448494

Goudarzi S, Babicz JT, Kabil O, Banerjee R, & Solomon EI (2018). Spectroscopic and Electronic Structure Study of ETHE1: Elucidating the Factors Influencing Sulfur Oxidation and Oxygenation in Mononuclear Nonheme Iron Enzymes. Journal of the American Chemical Society, 140(44), 14887–14902. 10.1021/JACS.8B09022 [PubMed: 30362717]

Kal S, & Que L (2017). Dioxygen activation by nonheme iron enzymes with the 2-His-1-carboxylate facial triad that generate high-valent oxoiron oxidants. Journal of Biological Inorganic Chemistry, 22(2–3), 339–365. 10.1007/s00775-016-1431-2 [PubMed: 28074299]

Kappock TJ, & Caradonna JP (1996). Pterin-Dependent Amino Acid Hydroxylases. Chemical Reviews, 96(7), 2659–2756. 10.1021/cr9402034 [PubMed: 11848840]

Kemsley JN, Mitić N, Zaleski KL, Caradonna JP, & Solomon EI (1999). Circular Dichroism and Magnetic Circular Dichroism Spectroscopy of the Catalytically Competent Ferrous Active Site of Phenylalanine Hydroxylase and Its Interaction with Pterin Cofactor. Journal of the American Chemical Society, 121(7), 1528–1536. 10.1021/JA9833063

Kemsley JN, Wasinger EC, Datta S, Mitić N, Acharya T, Hedman B, Caradonna JP, Hodgson KO, & Solomon EI (2003). Spectroscopic and Kinetic Studies of PKU–Inducing Mutants of Phenylalanine Hydroxylase: Arg158Gln and Glu280Lys. Journal of the American Chemical Society, 125(19), 5677–5686. 10.1021/ja029106f [PubMed: 12733906]

Krebs C, Galonić Fujimori D, Walsh CT, & Bollinger JM Jr. (2007). Non-Heme Fe(IV)–Oxo Intermediates. Accounts of Chemical Research, 40(7), 484–492. 10.1021/ar700066p [PubMed: 17542550]

Light KM, Hangasky JA, Knapp MJ, & Solomon EI (2014). First- and second-sphere contributions to Fe(ii) site activation by cosubstrate binding in non-heme Fe enzymes. Dalton Transactions, 43(4), 1505–1508. 10.1039/C3DT53201A [PubMed: 24292428]

Lipscomb JD (2008). Mechanism of extradiol aromatic ring-cleaving dioxygenases. Current Opinion in Structural Biology, 18(6), 644–649. 10.1016/J.SBI.2008.11.001 [PubMed: 19007887]

Loeb KE, Westre TE, Kappock TJ, Mitić N, Glasfeld E, Caradonna JP, Hedman B, Hodgson KO, & Solomon EI (1997). Spectroscopic characterization of the catalytically competent ferrous site of the resting, activated, and substrate-bound forms of phenylalanine hydroxylase. Journal of the American Chemical Society, 119(8), 1901–1915. 10.1021/JA962269H

Mitić N, Clay MD, Saleh L, Bollinger JM, & Solomon EI (2007). Spectroscopic and Electronic Structure Studies of Intermediate X in Ribonucleotide Reductase R2 and Two Variants: A Description of the FeIV-Oxo Bond in the FeIII–O–FeIV Dimer. Journal of the American Chemical Society, 129(29), 9049–9065. 10.1021/ja070909i [PubMed: 17602477]

Neese F, & Solomon EI (1999). MCD C-term signs, saturation behavior, and determination of band polarizations in randomly oriented systems with spin S ≥ 1/2. Applications to S = 1/2 and S = 5/2. Inorganic Chemistry, 38(8), 1847–1865. 10.1021/IC981264D [PubMed: 11670957]

Neidig ML, & Solomon EI (2005). Structure–function correlations in oxygen activating non-heme iron enzymes. Chemical Communications, 47, 5843–5863. 10.1039/B510233M

Park K, Li N, Kwak Y, Srnec M, Bell CB, Liu LV, Wong SD, Yoda Y, Kitao S, Seto M, Hu M, Zhao J, Krebs C, Bollinger JM, & Solomon EI (2017). Peroxide Activation for Electrophilic Reactivity by the Binuclear Non-heme Iron Enzyme AurF. Journal of the American Chemical Society, 139(20), 7062–7070. 10.1021/JACS.7B02997 [PubMed: 28457126]

Pavel EG, Kitajima N, & Solomon EI (1998). Magnetic Circular Dichroism Spectroscopic Studies of Mononuclear Non-Heme Ferrous Model Complexes. Correlation of Excited- and Ground-State Electronic Structure with Geometry. Journal of the American Chemical Society, 120(16), 3949–3962. 10.1021/JA973735L

Purpero V, & Moran GR (2007). The diverse and pervasive chemistries of the α-keto acid dependent enzymes. Journal of Biological Inorganic Chemistry, 12(5), 587–601. 10.1007/S00775-007-0231-0 [PubMed: 17431691]

Schatz PN, Mowery RL, & Krausz ER (1978). M.C.D./M.C.P.L. saturation theory with application to molecules in D ∞h and its subgroups. Molecular Physics, 35(6), 1537–1557. 10.1080/00268977800101151

Solomon EI, Brunold TC, Davis MI, Kemsley JN, Lee SK, Lehnert N, Neese F, Skulan AJ, Yang YS, & Zhou J (2000). Geometric and Electronic Structure/Function Correlations in Non-Heme Iron Enzymes. Chemical Reviews, 100(1), 235–349. 10.1021/cr9900275 [PubMed: 11749238]

Solomon EI, Deweese DE, & Babicz JT (2021). Mechanisms of O2 Activation by Mononuclear Non-Heme Iron Enzymes. Biochemistry, 60(46), 3497–3506. 10.1021/acs.biochem.1c00370 [PubMed: 34266238]

Solomon EI, & Hanson MA (2006). Bioinorganic Spectroscopy. In Solomon EI & Lever ABP (Eds.), Inorganic Electronic Structure and Spectroscopy (Vol. 2, pp. 1–129). John Wiley & Sons, Inc. https://www.wiley.com/en-us/Inorganic+Electronic+Structure+and+Spectroscopy%2C+Volume+II-p-9780471971146

Solomon EI, & Park K (2016). Structure/function correlations over binuclear non-heme iron active sites. Journal of Biological Inorganic Chemistry, 21(5), 575–588. 10.1007/s00775-016-1372-9 [PubMed: 27369780]

Solomon EI, Pavel EG, Loeb KE, & Campochiaro C (1995). Magnetic circular dichroism spectroscopy as a probe of the geometric and electronic structure of non-heme ferrous enzymes. Coordination Chemistry Reviews, 144, 369–460. 10.1016/0010-8545(95)01150-N

Srnec M, & Solomon EI (2017). Frontier Molecular Orbital Contributions to Chlorination versus Hydroxylation Selectivity in the Non-Heme Iron Halogenase SyrB2. Journal of the American Chemical Society, 139(6), 2396–2407. 10.1021/jacs.6b11995 [PubMed: 28095695]

Srnec M, Wong SD, Matthews ML, Krebs C, Bollinger JM, & Solomon EI (2016). Electronic Structure of the Ferryl Intermediate in the α-Ketoglutarate Dependent Non-Heme Iron Halogenase SyrB2: Contributions to H Atom Abstraction Reactivity. Journal of the American Chemical Society, 138, 5110–5122. 10.1021/jacs.6b01151 [PubMed: 27021969]

Stephens PJ (1976). Magnetic Circular Dichroism. In Advances in Chemical Physics (pp. 197–264). 10.1002/9780470142547.ch4

Sutherlin KD, Rivard S, B, Böttger H, L, Liu V, L, S. Rogers, Srnec M, Park K, Yoda Y, Kitao S, Kobayashi Y, Saito M, Seto M, Hu M, Zhao J, Lipscomb JD, & Solomon EI. (2018). NRVS Studies of the Peroxide Shunt Intermediate in a Rieske Dioxygenase and Its Relation to the Native FeII O2 Reaction. Journal of the American Chemical Society, 140(16), 5544–5559. 10.1021/jacs.8b01822 [PubMed: 29618204]

Sutherlin KD, Wasada-Tsutsui Y, Mbughuni MM, Rogers MS, Park K, Liu LV, Kwak Y, Srnec M, Böttger LH, Frenette M, Yoda Y, Kobayashi Y, Kurokuzu M, Saito M, Seto M, Hu M, Zhao J, Alp EE, Lipscomb JD, & Solomon EI (2018). Nuclear Resonance Vibrational Spectroscopy Definition of O2 Intermediates in an Extradiol Dioxygenase: Correlation to Crystallography and Reactivity. Journal of the American Chemical Society, 140(48), 16495–16513. 10.1021/jacs.8b06517 [PubMed: 30418018]

Thomson AJ, & Johnson MK (1980). Magnetization curves of haemoproteins measured by low-temperature magnetic-circular-dichroism spectroscopy. Biochemical Journal, 191(2), 411–420. 10.1042/bj1910411 [PubMed: 6263246]

Vaillancourt FH, Bolin JT, & Eltis LD (2006). The Ins and Outs of Ring-Cleaving Dioxygenases. Critical Reviews in Biochemistry and Molecular Biology, 41(4), 241–267. 10.1080/10409230600817422 [PubMed: 16849108]

Whittaker JW, & Solomon EI (1988). Spectroscopic studies on ferrous nonheme iron active sites: magnetic circular dichroism of mononuclear iron sites in superoxide dismutase and lipoxygenase. Journal of the American Chemical Society, 110(16), 5329–5339. 10.1021/ja00224a017
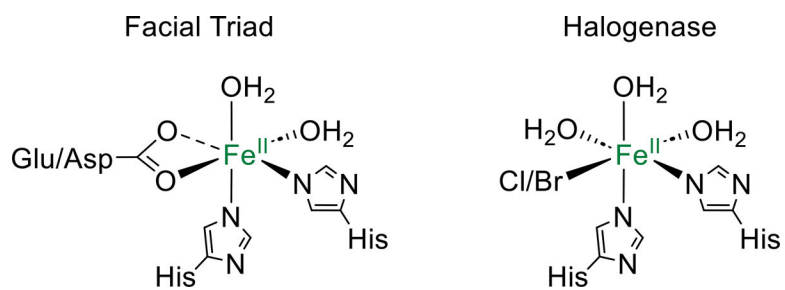
Figure 1.
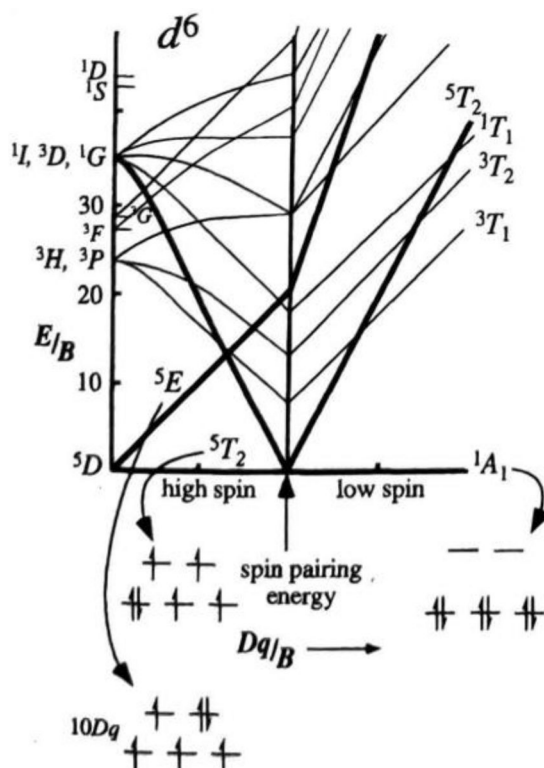Schematic structures of non-heme ferrous active sites.

Figure 2.
Tanabe-Sugano Diagram quantifying the energy the states of a d^6 transition metal ion in an octahedral ligand field in terms of Dq and B. Used with permission from John Wiley & Sons from (Solomon & Hanson, 2006).
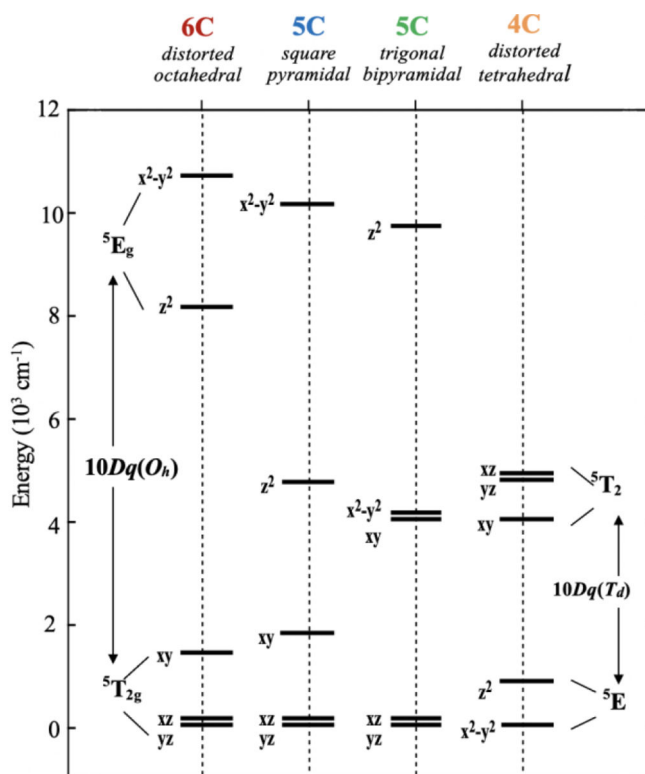
Figure 3.
Ligand field splitting of the high spin quintet d^6 LF states with coordination number
and structure. Adapted with permission from Solomon, E. I., Brunold, T. C., Davis, M.
I., Kemsley, J. N., Lee, S. K., Lehnert, N., Neese, F., Skulan, A. J., Yang, Y. S., &
Zhou, J. (2000). Geometric and Electronic Structure/Function Correlations in Non-Heme
Iron Enzymes. *Chemical Reviews*, *100*(1), 235–349. https://doi.org/10.1021/cr9900275
(Solomon et al., 2000). Copyright 2000 American Chemical Society.
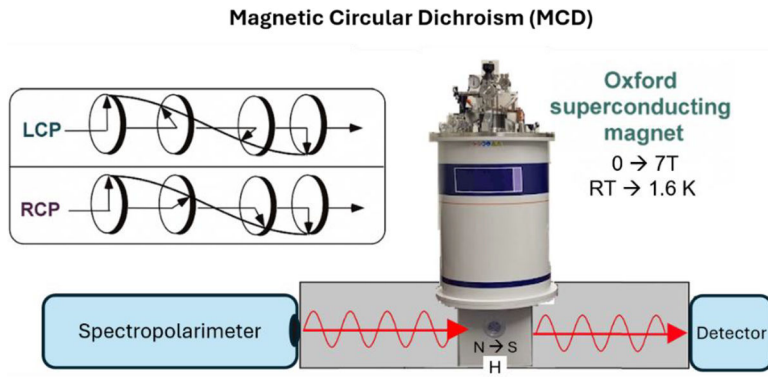
Figure 4.
Experimental configuration for VTVH MCD.
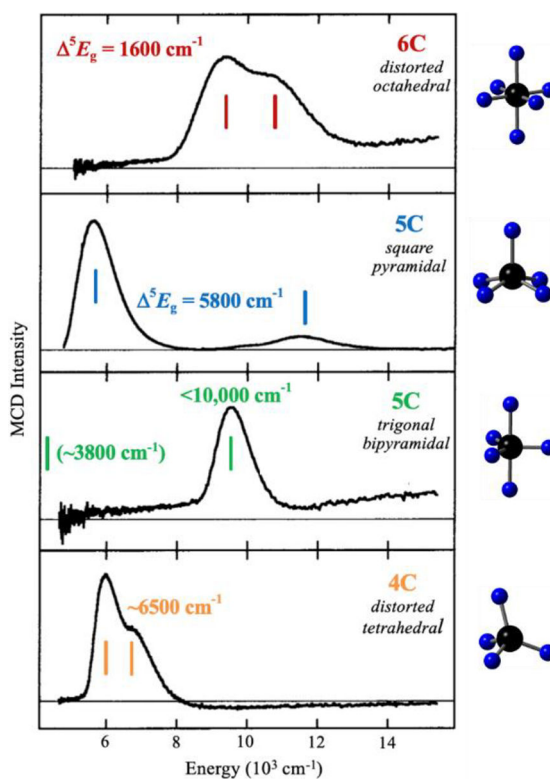
Figure 5.
LT MCD spectra of representative structurally defined Fe^{II} model complexes. (A) 6C, octahedral $[Fe(H_2O)_6](SiF_6)$. (B) 5C, square-pyramidal $[Fe(HB(3,5-^iPr_2pz)_3)(OAc)]$. (C) 5C, trigonal-bipyramidal $[Fe(tris(2-(dimethylamino)ethyl)amine)Br]^+$. (D) 4C, tetrahedral $[Fe(HB(3,5-^iPr_2pz)_3)(Cl)]$. Adapted with permission from Pavel, E. G., Kitajima, N., & Solomon, E. I. (1998). Magnetic Circular Dichroism Spectroscopic Studies of Mononuclear Non-Heme Ferrous Model Complexes. Correlation of Excited- and Ground-State Electronic Structure with Geometry. *Journal of the American Chemical Society*, *120*(16), 3949–3962. https://doi.org/10.1021/JA973735L (Pavel et al., 1998). Copyright 1998 American Chemical Society.
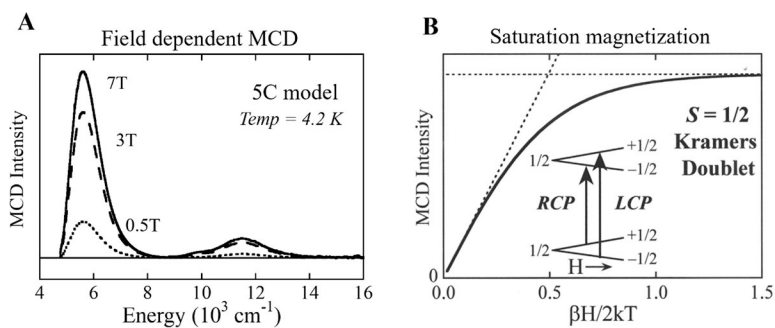
Figure 6.
(A) Field dependence of the MCD signal from the 5C complex in Figure 5. (B) Saturation magnetization MCD for an $S = 1/2$ Kramers doublet; signal as a function of field and temperature. Inset shows Kramers doublet in a magnetic field and MCD allowed transitions. Adapted with permission from Solomon, E. I., Brunold, T. C., Davis, M. I., Kemsley, J. N., Lee, S. K., Lehnert, N., Neese, F., Skulan, A. J., Yang, Y. S., & Zhou, J. (2000). Geometric and Electronic Structure/Function Correlations in Non-Heme Iron Enzymes. *Chemical Reviews*, *100*(1), 235–349. https://doi.org/10.1021/cr9900275 (Solomon et al., 2000). Copyright 2000 American Chemical Society.
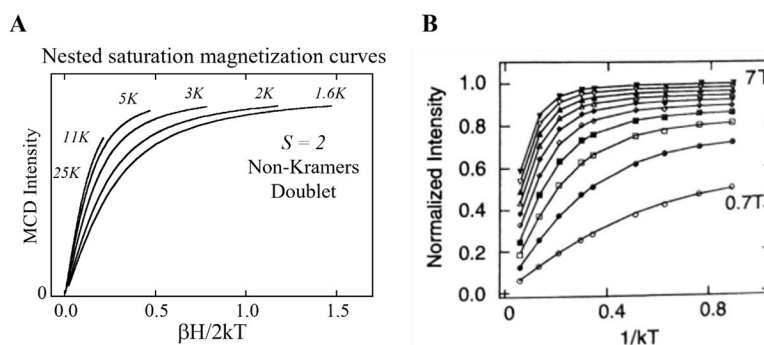
Figure 7.
Saturation magnetization data and fits using equation 2 for the ferrous 5C complex in Figure 5 and 6A recorded at 6,000 cm^{-1}. (A) Nesting behavior shown in plot of intensity versus βH/2kT; (B) and intensity versus temperature for fixed field increments. Adapted from Solomon, E. I., Pavel, E. G., Loeb, K. E., & Campochiaro, C. (1995). Magnetic circular dichroism spectroscopy as a probe of the geometric and electronic structure of non-heme ferrous enzymes. *Coordination Chemistry Reviews*, *144*, 369–460. https://doi.org/10.1016/0010-8545(95)01150-N (Solomon et al., 1995) with permission from Elsevier.
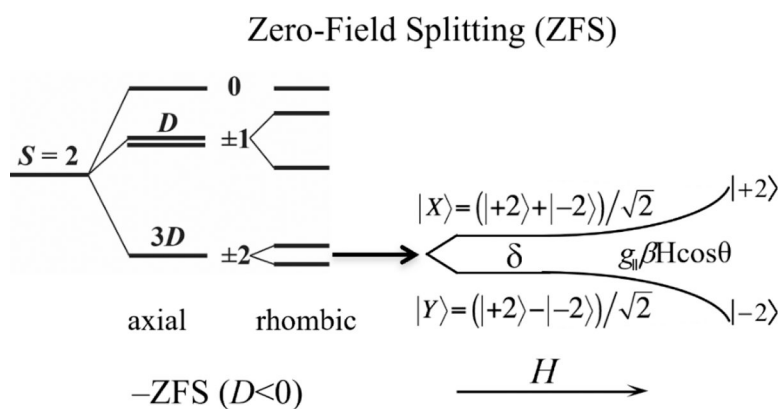
Figure 8.

Energy splittings of the $S = 2$ sublevels for an axial $-ZFS$ and a rhombic distortion and then magnetic field splitting and mixing of an $MS = \pm2$ non-Kramers doublet. Adapted with permission from Campochiaro, C., Pavel, E. G., & Solomon, E. I. (1995). Saturation Magnetization Magnetic Circular Dichroism Spectroscopy of Systems with Positive Zero-Field Splittings: Application to FeSiF6·6H2O. *Inorganic Chemistry*, *34*(18), 4669–4675. https://doi.org/10.1021/IC00122A025 (Campochiaro et al., 1995). Copyright 1995 American Chemical Society.
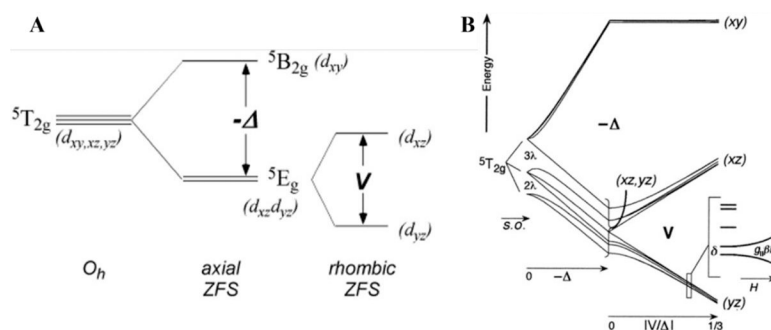
Figure 9.
LF splitting of the t_2 dπ orbitals (A), including SOC (B) and the Zeeman effect (inset). Adapted from (A) Solomon, E. I., & Hanson, M. A. (2006). Bioinorganic Spectroscopy. In E. I. Solomon & A. B. P. Lever (Eds.), *Inorganic Electronic Structure and Spectroscopy* (Vol. 2, pp. 1–129). John Wiley & Sons, Inc. https://www.wiley.com/en-us/Inorganic+Electronic+Structure+and+Spectroscopy%2C+Volume+II-p-9780471971146 (Solomon & Hanson, 2006) with permission from John Wiley & Sons and (B) Solomon, E. I., Pavel, E. G., Loeb, K. E., & Campochiaro, C. (1995). Magnetic circular dichroism spectroscopy as a probe of the geometric and electronic structure of non-heme ferrous enzymes. *Coordination Chemistry Reviews*, *144*, 369–460. https://doi.org/10.1016/0010-8545(95)01150-N (Solomon et al., 1995) with permission from Elsevier.
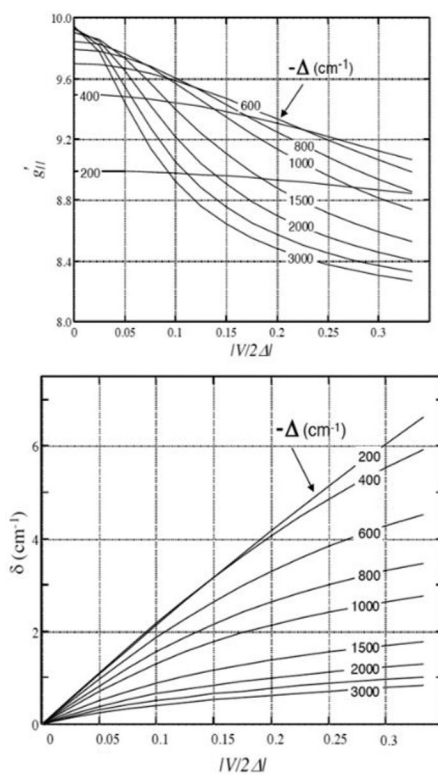
Figure 10.
Correlations of the $g_∥$ (top) and δ (bottom) with the axial ( ) and rhombic (V) LF splitting of the t_2 dπ orbitals. Adapted from Solomon, E. I., Pavel, E. G., Loeb, K. E., & Campochiaro, C. (1995). Magnetic circular dichroism spectroscopy as a probe of the geometric and electronic structure of non-heme ferrous enzymes. *Coordination Chemistry Reviews, 144*, 369–460. https://doi.org/10.1016/0010-8545(95)01150-N (Solomon et al., 1995) with permission from Elsevier.
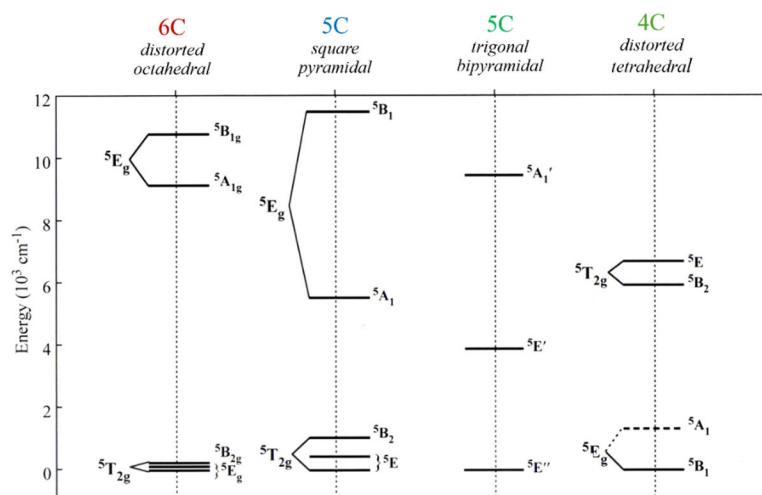
Figure 11.
Experimental Ligand-Field splittings of the five d orbitals for the complexes in Figure 5. Adapted with permission from Pavel, E. G., Kitajima, N., & Solomon, E. I. (1998). Magnetic Circular Dichroism Spectroscopic Studies of Mononuclear Non-Heme Ferrous Model Complexes. Correlation of Excited- and Ground-State Electronic Structure with Geometry. *Journal of the American Chemical Society*, *120*(16), 3949–3962. https://doi.org/10.1021/JA973735L (Pavel et al., 1998). Copyright 1998 American Chemical Society.
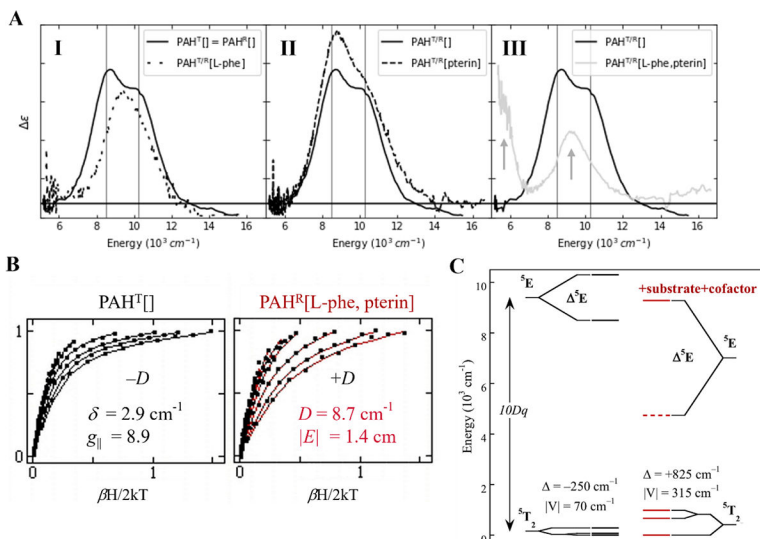
Figure 12.
MCD elucidation of the cosubstrate activation mechanism of the Fe(II) site in PAH. (A) LT MCD, (B) VTVH MCD, and (C) experimentally determined LF splitting of the d orbitals. Adapted with permission from Kemsley, J. N., Miti , N., Zaleski, K. L., Caradonna, J. P., & Solomon, E. I. (1999). Circular Dichroism and Magnetic Circular Dichroism Spectroscopy of the Catalytically Competent Ferrous Active Site of Phenylalanine Hydroxylase and Its Interaction with Pterin Cofactor. *Journal of the American Chemical Society*, *121*(7), 1528–1536. https://doi.org/10.1021/JA9833063 (Kemsley et al., 1999) and Loeb, K. E., Westre, T. E., Kappock, T. J., Miti , N., Glasfeld, E., Caradonna, J. P., Hedman, B., Hodgson, K. O., & Solomon, E. I. (1997). Spectroscopic characterization of the catalytically competent ferrous site of the resting, activated, and substrate-bound forms of phenylalanine hydroxylase. *Journal of the American Chemical Society*, *119*(8), 1901–1915. https://doi.org/10.1021/JA962269H (Loeb et al., 1997). Copyright 1999 and 1997 American Chemical Society.
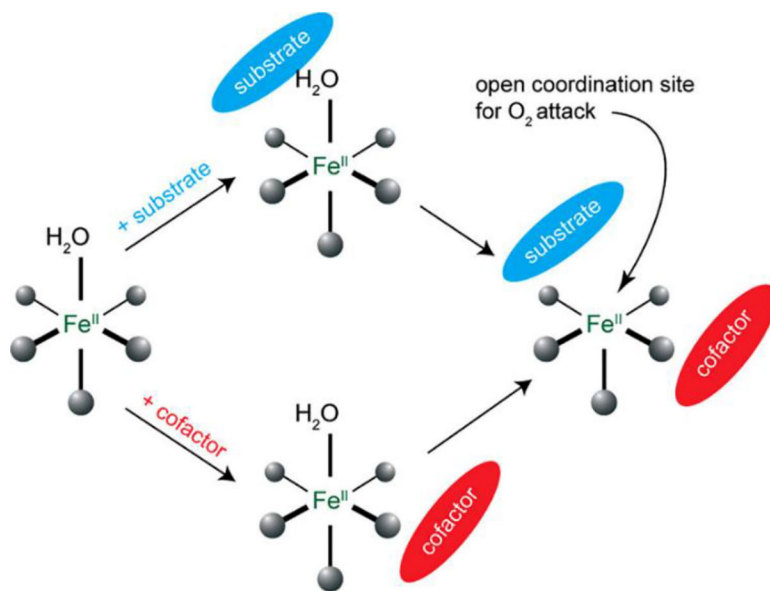
Figure 13.
General Mechanistic Strategy for Cofactor-Dependent NHFe Enzymes. Adapted with permission from Solomon, E. I., Deweese, D. E., & Babicz, J. T. (2021). Mechanisms of O2 Activation by Mononuclear Non-Heme Iron Enzymes. *Biochemistry*, *60*(46), 3497–3506. https://doi.org/10.1021/acs.biochem.1c00370 (Solomon et al., 2021). Copyright 2021 American Chemical Society.

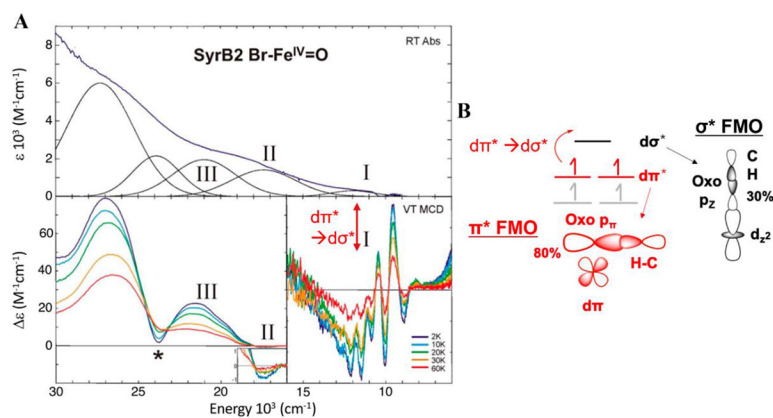**Figure 14.**
(A) Absorption (top) and VT MCD spectra (bottom) of SyrB2 Br–Fe^{IV}=O. Transition I is the dπ* →dσ* LF transition, and II and III are oxo to iron charge transfer transitions. The * indicates a minor heme contaminant in the sample. Adapted with permission from Srnec, M., Wong, S. D., Matthews, M. L., Krebs, C., Bollinger, J. M., & Solomon, E. I. (2016). Electronic Structure of the Ferryl Intermediate in the α-Ketoglutarate Dependent Non-Heme Iron Halogenase SyrB2: Contributions to H Atom Abstraction Reactivity. *Journal of the American Chemical Society*, *138*, 5110–5122. https://doi.org/10.1021/jacs.6b01151 (Srnec et al., 2016). Copyright 2016 American Chemical Society. (B) Schematic showing the relevant FMOs and the orbitals participating in the dπ* →dσ* LF transition.

Table 1.

Major classes of non-heme ferrous enzymes. Adapted with permission from Solomon, E. I., Deweese, D. E., & Babicz, J. T. (2021). Mechanisms of O2 Activation by Mononuclear Non-Heme Iron Enzymes. *Biochemistry*, *60*(46), 3497–3506. https://doi.org/10.1021/acs.biochem.1c00370 (Solomon et al., 2021). Copyright 2021 American Chemical Society.